Journal of Biomechanics 158 (2023) 111759

Contents lists available at ScienceDirect

Journal of Biomechanics

journal homepage: www.elsevier.com/locate/jbiomech

Towards Reduced Order Models via Robust Proper Orthogonal Decomposition to capture personalised aortic haemodynamics

Chotirawee Chatpattanasiri [a], Gaia Franzetti [a], Mirko Bonfanti [a], Vanessa Diaz-Zuccarini [a,b], Stavroula Balabani [a,*]

[a] Department of Mechanical Engineering, University College London, London, UK
[b] Wellcome/EPSRC Centre for Interventional and Surgical Sciences (WEISS), Department of Medical Physics and Biomedical Engineering, University College London, London, UK

ARTICLE INFO

Keywords:
Aortic haemodynamics
Particle image velocimetry
Computational fluid dynamics
Reduced Order Model
Proper orthogonal decomposition
Robust principle component analysis
Patient-specific modelling

ABSTRACT

Data driven, reduced order modelling has shown promise in tackling the challenges associated with computational and experimental haemodynamic models. In this work, we focus on the use of Reduced Order Models (ROMs) to reconstruct velocity fields in a patient-specific dissected aorta, with the objective being to compare the ROMs obtained from Robust Proper Orthogonal Decomposition (RPOD) to those obtained from the traditional Proper Orthogonal Decomposition (POD). POD and RPOD are applied to *in vitro*, haemodynamic data acquired by Particle Image Velocimetry and compare the decomposed flows to those derived from Computational Fluid Dynamics (CFD) data for the same geometry and flow conditions. In this work, PIV and CFD results act as surrogates for clinical haemodynamic data e.g. MR, helping to demonstrate the potential use of ROMS in real clinical scenarios. The flow is reconstructed using different numbers of POD modes and the flow features obtained throughout the cardiac cycle are compared to the original Full Order Models (FOMs).

Robust Principal Component Analysis (RPCA), the first step of RPOD, has been found to enhance the quality of PIV data, allowing POD to capture most of the kinetic energy of the flow in just two modes similar to the numerical data that are free from measurement noise. The reconstruction errors differ along the cardiac cycle with diastolic flows requiring more modes for accurate reconstruction. In general, modes 1–10 are found sufficient to represent the flow field. The results demonstrate that the coherent structures that characterise this aortic dissection flow are described by the first few POD modes suggesting that it is possible to represent the macroscale behaviour of aortic flow in a low-dimensional space; thus significantly simplifying the problem, and allowing for more computationally efficient flow simulations or machine learning based flow predictions that can pave the way for translation of such models to the clinic.

1. Introduction

Restoring flow and functionality is the main objective of clinicians when performing vascular interventions. The ability to visualise biomechanical flows, either by *in vitro* experiments or Computational Fluid Dynamics (CFD), can provide invaluable information for clinical support, disease progression predictions and surgical treatment planning (Bonfanti et al., 2020) by helping design tailored interventions, personalise devices or explore clinical scenarios for future treatment, for example. Application of such tools has been successfully demonstrated in several pathologies, such as aortic dissection (Bonfanti et al., 2020; Franzetti et al., 2022; Stokes et al., 2021, 2023), coronary artery disease (Javadzadegan et al., 2018), valve prosthesis (Hellmeier et al., 2018), aortic aneurysm (Febina et al., 2018) and congenital heart disease (Rigatelli et al., 2021). Both *in vitro* and *in silico* haemodynamic approaches are subject to certain limitations. In CFD for example, a compromise between model accuracy and complexity has often need to be made (Bonfanti et al., 2018). Over-simplifications of the geometrical domain and boundary conditions can lead to non-realistic results. However, increasing the model complexity further complicates the solution, increasing the computational time and often introducing or increasing uncertainty. High computational cost represents a problem for the clinical translation of these numerical models, especially when considering the time-scales of *acute* pathological stages (i.e. days rather than weeks or months) and the limited time available in clinics to make full use of CFD as realistic tool for pre-interventional planning.

* Corresponding author.
E-mail address: s.balabani@ucl.ac.uk (S. Balabani).

https://doi.org/10.1016/j.jbiomech.2023.111759
Accepted 7 August 2023
Available online 10 August 2023

To address this problem, Reduced Order Models (ROMs) have been extensively studied to accelerate calculations of fluid dynamic problems (Quarteroni and Rozza, 2007). ROMs replace large-scale problems with less complex ones that can be solved with significantly less time and resources, while maintaining acceptable accuracy. If we were able to extract ROMS from clinical measurement modalities (e.g MR) with a view to use them as input to train fast haemodynamic tools this would address the limitations of traditional CFD and completely transform the use of simulation tools for haemodynamic computations in the clinic. Many methods have been developed to extract ROMs from high-fidelity data, such as Proper Orthogonal Decomposition (POD) (Liang et al., 2002; Brunton and Kutz, 2019; Arzani and Dawson, 2021), Proper Generalised Decomposition (PGD) (Chinesta et al., 2011), Dynamic Mode Decomposition (Arzani and Dawson, 2021; Schmid, 2021), Krylov subspace (Farahbakhsh, 2020), and the recently developed neural network based method, Autoencoder (Wang et al., 2016; Murata et al., 2020; Eivazi et al., 2022; Liang et al., 2020).

Among these methods, POD is arguably the most popular.[1] POD reduces the dimensionality of a system by projecting it onto a set of orthogonal Reduced Basis (POD modes). It identifies the dominant modes in a flow, breaking it down into large and small-scale structures. With the goal of quantifying different flow regimes and developing computationally-efficient ROMs, POD has been applied to several vascular flow studies, either using numerical CFD data or experimentally-derived velocity fields acquired via Particle Image Velocimetry (PIV). For instance, Kefayati and Poepping (2013) used a combination of PIV and POD to study transitional flows in stenosed silicon models; Byrne et al. (2014) introduced entropy to quantify the flow instability of intracranial aneurysm using POD; Ballarin et al. (2016) developed a framework for the study of haemodynamics in three-dimensional patient-specific configurations of coronary artery bypass grafts. More recently, Di Labbio and Kadem (2019) compared POD and DMD reconstructions of *in vitro* ventricular flow in a healthy left ventricle and multiple severities of aortic regurgitation, and Han et al. (2020) applied POD to estimate the flow-induced WSS in computational models of abdominal aortic aneurysm.

Robust Proper Orthogonal Decomposition (RPOD) or Robust Principal Component Analysis (RPCA) is an extension of the Proper Orthogonal Decomposition (POD) method, designed to handle noisy or corrupted data commonly found in clinical and experimental datasets (Arzani and Dawson, 2021; Scherl et al., 2020). However, its application in fluid flows, especially in the field of physiological flows, is limited. Previous studies include Scherl et al. (2020), who implemented RPOD filtering in a turbulent channel flow simulation to extract coherent flow structures from the de-noised low-rank matrix, and Baghaie (2019), who applied RPOD to filter out background motion from raw PIV sequences.

In this work, and in the context of using ROMS for clinical application, we will use PIV and CFD results as surrogates for clinical haemodynamic data to demonstrate the potential of the RPOD algorithm when compared to traditional POD for decomposing aortic flow data and constructing ROMs. The RPOD method was applied to the patient-specific aortic, PIV-derived, flow field described in our previous work (Bonfanti et al., 2020; Franzetti et al., 2022). The eigenflows generated are compared to those derived by POD applied to the same data set as well as CFD-derived flow fields for the same geometry. ROMs are then successfully used to reconstruct the original flow fields and their potential for personalised haemodynamic modelling is discussed.

2. Materials and methods

A schematic of the approach followed in this work is shown in Fig. 1. We have previously characterised and fully validated the flow in a patient-specific dissected aorta both experimentally (using PIV) and numerically (using CFD) (Franzetti et al., 2022; Bonfanti et al., 2020) (black part of the figure). These datasets comprise the Full Order Models. The RPCA algorithm was applied to the PIV velocity field to create a de-noised dataset, which we call RPCA velocity field (blue part of the figure).

The state reduction of the problem was then achieved by projecting the CFD, PIV, and RPCA velocity fields onto their POD bases to reduce the dimensionality of the problem (Galerkin projection). ROMs were identified, ROM-derived flow fields were reconstructed (green part of the figure) and compared to the FOMs. The errors introduced when considering a lower dimensional model were assessed (Yellow part of the figure).

2.1. Patient-specific model

The study is based on clinical data acquired from an adult male with a Type B aortic dissection, a pathology that occurs when a tear in the vessel wall allows blood to flow within the layers of the aorta, leading to the formation of two separate flow-channels, the true and the false lumen. The dataset was acquired as part of an ethically-approved protocol at the Leeds General Infirmary (NHS Health Research Authority, ref: 12/YH/0551; Leeds Teaching Hospitals NHS Trust, ref: 788/RADRES/16), and appropriate concent was obtained from the patient. The aortic model was created from the patient CT scans using a semi-automated segmentation tool based on thresholding operations, implemented in ScanIP (Synopsys, Mountain View, CA, USA). It includes one inlet and four outlets: the brachiocephalic trunk (BT), left common carotid (LCC), left subclavian artery (LSA), and descending aorta (DA). A rigid, transparent phantom was manufactured by 3D printing technology (Materialise, Belgium) to enable the flow field measurements described below.

2.2. Experimental setup and PIV measurements

The phantom was connected to a custom-made pulsatile flow circuit which comprised a computer controlled pulsatile pump and left ventricle simulator, tunable 3-element Windkessel (3WKs) model at each aortic outlet (Fig. 2) and an atrial reservoir (Franzetti et al., 2019). The mock loop components were informed by clinical data to reproduce personalised, accurate haemodynamics (Franzetti et al., 2022). A blood mimicking fluid comprising a potassium thiocyanate (KSCN) water solution (63% by weight) was used, matching the refractive index of the phantom. Patient-specific flow and pressure waveforms were introduced at the inlets and outlets of the aortic model as illustrated in Bonfanti et al. (2020) and Franzetti et al. (2022). To perform the PIV measurements, the flow was seeded with fluorescent microparticles with a mean diameter of 10 μm, injected into the flow upstream of the phantom and allowed to disperse uniformly within the aortic model. The flow was illuminated by a pulsed Nd:YAG laser (Litron Lasers, Bernoulli, UK) emitting 532 nm wavelength light. Particle image pairs were acquired with a CCD camera (Imperx, USA) at a sampling rate of 22 Hz (the pulsatile flow has a frequency of 1.2 Hz) with a resolution of 4000 × 3000 pixels with a time interval of 1 ms. 10 cardiac cycles were recorded.[2] Velocity fields were generated using the Fast Fourier transform based cross-correlation algorithm, implemented with a three-pass technique starting with an interrogation area of 64 × 64 pixels and ending with an area of 32 × 32 pixels, overlapping by 50%. Lastly, post-processing was performed using custom developed MATLAB (MathWorks Inc., USA) functions. The measurement error, estimated from mass conservation, is 5.32% (Franzetti et al., 2022).

[1] POD is mathematically equivalent to Principal Component Analysis (PCA) (Liang et al., 2002).

[2] The flow converged with less than 1.6% cycle-to-cycle variation (Bonfanti et al., 2020; Franzetti et al., 2022).

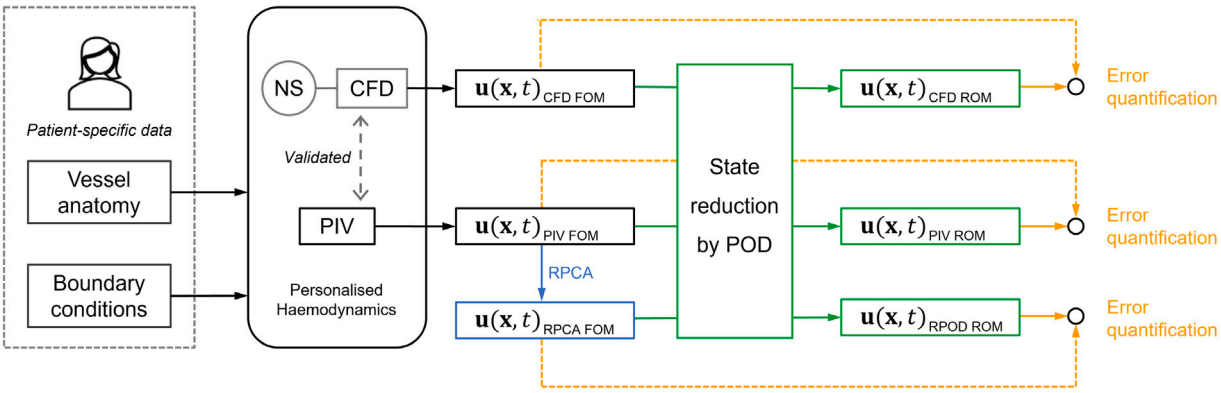

Fig. 1. Schematic of the approach followed in this work, comprising four phases. First, the development of Full order models (FOMs), was described in previous works by the authors (Bonfanti et al., 2020; Franzetti et al., 2022) and led to the experimental PIV model and a computational CFD one (black part of the figure). In the second phase, RPCA is applied to the PIV velocity field to create a de-noised RPCA velocity field (blue part of the figure). The third phase involves the creation of ROMs based on the original velocity fields through POD (green part of the figure). In the last phase, the reconstructed velocity fields were compared to their respective original FOMs, the errors involved were assessed (yellow part of the figure). (For interpretation of the references to color in this figure legend, the reader is referred to the web version of this article.)

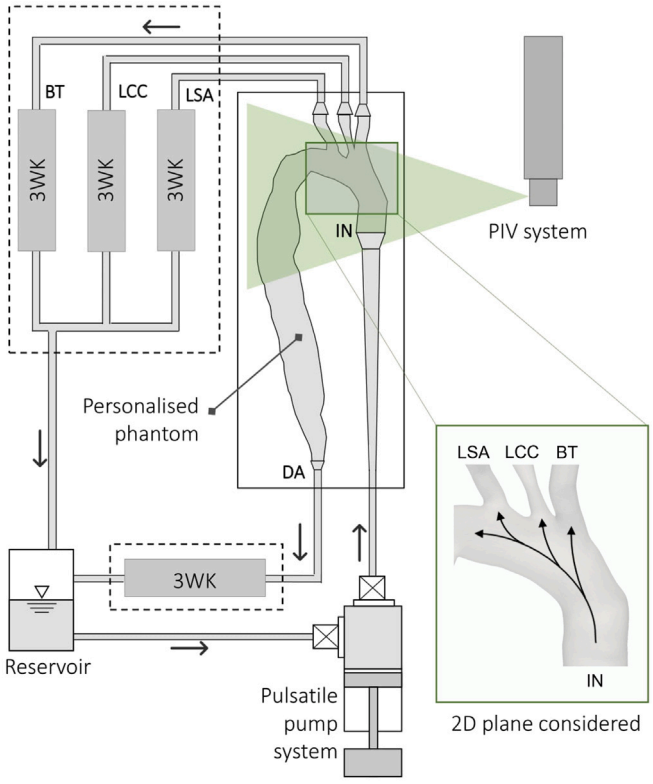

Fig. 2. Schematic of the experimental setup. The rig comprises a pulsatile pump system to provide the patient-specific inlet flow rate into the aortic phantom; four 3-elements Windkessel models (3WKs) – one for each of the outlets: brachiocephalic trunk (BT), left common carotid (LCC), left subclavian artery (LSA), and descending aorta (DA) – and an aortic reservoir. The 2D plane where the PIV acquisitions considered in this work were performed is also represented. Superimposed arrows qualitatively indicate the direction of the flow during systole.

Details about the components of the mock circulatory loop and the experimental procedures can be found in our previous work (Franzetti et al., 2019, 2022). Here, the PIV-derived velocities obtained on a cross-sectional plane of the aortic arch (shown in Fig. 2), consisting of 10 cardiac cycles with 18 snapshots per cycle, i.e. 180 snapshots in total, were used. This minimises the risk of bias introduced by using a single cycle, and better represents flow behaviour.

2.3. PIV data enhancement by RPCA

Robust Principal Component Analysis (RPCA) or Robust Proper Orthogonal Decomposition (RPOD) is an extension of PCA or POD that separate an original data matrix ($\mathbf{U}$) into a sparse noise matrix ($\mathbf{S}$) and a low-rank matrix containing coherent information ($\mathbf{L}$) using the following equation:

$$\mathbf{U} = \mathbf{L} + \mathbf{S}. \tag{1}$$

RPCA is known for its ability to handle noisy data (Scherl et al., 2020; Arzani and Dawson, 2021; Candès et al., 2011; Brunton and Kutz, 2019) and is a good candidate to enhance the PIV data prior to further analysis. The implementation of RPCA involves solving a constrained minimisation equation:

$$\min_{\mathbf{L},\mathbf{S}} \left(\text{rank}(\mathbf{L}) + \|\mathbf{S}\|_0 \right) \text{ subject to } \mathbf{U} = \mathbf{L} + \mathbf{S} \tag{2}$$

where $\|\mathbf{S}\|_0$ represents the zero norm of $\mathbf{S}$, which is the summation of non-zero elements in $\mathbf{S}$. A convex relaxation (2) form of the problem is used:

$$\min_{\mathbf{L},\mathbf{S}} \left(\|\mathbf{L}\|_* + \lambda_0 \|\mathbf{S}\|_1 \right) \text{ subject to } \mathbf{U} = \mathbf{L} + \mathbf{S} \tag{3}$$

where $\|\mathbf{L}\|_*$ represents the nuclear norm of $\mathbf{L}$, which is the summation of all the singular values of $\mathbf{L}$, and $\|\mathbf{S}\|_1$ denotes the first norm of $\mathbf{S}$. λ_0 is a hyperparameter introduced as part of the relaxation given by $\lambda_0 = \lambda_1 / \sqrt{\max(m,n)}$ where $m \times n$ is the dimension of $\mathbf{U}$ and $\lambda_1 = 1$ in the original paper (Candès et al., 2011). Scherl et al. (2020) suggested that λ_1 can also be used as a tuning parameter: high λ_1 yields high sparsity of $\mathbf{S}$, and low λ_1 gives low rank of $\mathbf{L}$. For simplicity, λ_1 is kept at 1 in this study. Eq. (3) can be solved using the Augmented Lagrange Multiplier (ALM) algorithm together with the Alternating Direction Method (ADM) (Brunton and Kutz, 2019).

RPCA is used here as a de-noising tool to improve the PIV velocity field and thus is not applied to the CFD data. It is important to note that, because RPCA distinguishes outliers from coherent data, it may struggle when data points are scarce, blurring the difference between outliers and coherent information. Therefore, all acquired PIV snapshots (180) were used.

The term 'RPCA velocity field' is used to denote the PIV velocity field that has been de-noised by the RPCA process, whereas the term 'RPOD' refers to the implementation of POD after RPCA.

2.4. Numerical simulation

The CFD data is taken from a previous study by our group (Bonfanti et al., 2020). A Reynolds-averaged Navier–Stokes (RANS) model was

employed in this study to match the experimental inlet conditions since it is very difficult to achieve truly laminar flow in experiments. While RANS models are known to present certain limitations, such as not capturing unsteady turbulence fluctuations and assuming fully turbulent flow, they offer a good compromise between accuracy and computational efficiency in comparison to more resource-intensive methods like Large Eddy Simulation (LES) and Direct Numerical Simulation (DNS); they were hence selected for this study and showed good agreement with the experimental data (Bonfanti et al., 2020). ANSYS-CFX 19.0 (ANSYS, USA) was used to solve the 3D incompressible Navier–Stokes and continuity equations, simulating the flow conditions of the PIV experiment. The vessel geometry is the same as the one used to make the phantom, with the walls assumed rigid. All boundary conditions are set to match those from the experiments. The experimental inlet flow rate waveform is imposed with a flat velocity profile. 3WKs models are coupled at the outlets. The fluid is assumed to be Newtonian, with the properties of the KSCN solution. The shear stress transport (SST) turbulence model is chosen with the turbulence intensity of 1% prescribed at the inlet.

The simulations run for 3 cardiac cycles and the first two cycles were excluded from the analysis as they contain transient behaviour influenced by the initial conditions and numerical setup. Unlike in the flow field obtained from PIV experiments, in the case of CFD, once the simulations have converged to the periodic steady state, every cycle is identical. Therefore, a single cycle is used in our study as is commonly done in most patient specific simulations (Bonfanti et al., 2020; Stokes et al., 2023). The flow field on the 2D aortic arch plane corresponding to the experimental one used here was exported to MATLAB via CFD-Post (ANSYS).

2.5. Proper orthogonal decomposition

The POD method decomposes the flow into a set of *modes* arranged depending on their energy content. The higher energy modes represent the coherent structures in the flow; as a result POD has been applied widely to turbulent flows to extract dominant structures. A detailed description of POD can be found in Berkooz et al. (1993) and in the textbook by Brunton and Kutz (2019). Only a brief overview is provided here.

POD is implemented using the method of *snapshots*. Consider a 2D velocity field of $n = N_x \times N_y$ spatial velocity vectors (u, v) on a Cartesian grid x, y and a total number of m instantaneous velocity fields or *snapshots*. POD decomposes the fluctuating part of the velocity field $\mathbf{u}'(x, y, t)$ into a set of spatial functions $\mathbf{\Phi}_i(x, y)$, called the *POD modes*, weighted by time-dependent coefficients $a_i(t)$ so that:

$$\mathbf{u}'(x, y, t) = \sum_{i=1}^{N} a_i(t)\mathbf{\Phi}_i(x, y) \tag{4}$$

where i denotes the mode number, and N denotes the total number of modes.[3]

To perform the decomposition (Eq. (4)), the time-averaged velocity $\overline{\mathbf{u}(x, y)}$ is first subtracted from each instantaneous velocity field, obtaining a set of m fluctuating velocity fields $\mathbf{u}'(x, y, t)$. The dataset is then rearranged in a $2n \times m$ *snapshot matrix* $\mathbf{U}$:

$$\mathbf{U} = \begin{pmatrix} u'_{1,1} & u'_{1,2} & \cdots & u'_{1,m} \\ \vdots & \vdots & \ddots & \vdots \\ u'_{n,1} & u'_{n,2} & \cdots & u'_{n,m} \\ v'_{1,1} & v'_{1,2} & \cdots & v'_{1,m} \\ \vdots & \vdots & \ddots & \vdots \\ v'_{n,1} & v'_{n,2} & \cdots & v'_{n,m} \end{pmatrix} \tag{5}$$

[3] Note that $\mathbf{u}'$ in Eq. (4) includes both the periodic variation around the mean and the turbulence fluctuation.

and Singular Value Decomposition (SVD) is applied:

$$\mathbf{U} = \mathbf{\Phi}\mathbf{\Sigma}\mathbf{\Psi}^* \tag{6}$$

where $\mathbf{\Phi}$ and $\mathbf{\Psi}$ are the left and right singular vectors of $\mathbf{U}$, respectively and $\mathbf{\Psi}^*$ is the conjugate transpose of $\mathbf{\Psi}$. The singular matrix $(\mathbf{\Sigma})$ contains the singular values (σ_i) of $\mathbf{U}$ which rank in descending order, and are directly linked to the portion of kinetic energy (λ_i) contained in the POD modes $(\mathbf{\Phi}_i)$, i.e. $\lambda_i = \sigma_i^2$. Therefore, POD modes are ranked according to their energy content, with the first mode having the highest energy, and the last the lowest. The energy fraction of the ith mode E_i, is defined as

$$E_i = \frac{\lambda_i}{\sum_{i=1}^{N} \lambda_i} \tag{7}$$

The temporal POD coefficients can be obtained by projecting $\mathbf{U}$ onto $\mathbf{\Phi}_i$:

$$a_i(t) = \mathbf{\Phi}_i^* \mathbf{U} \tag{8}$$

The total number of POD modes (N) is the rank of $\mathbf{U}$, which is usually equal to the number of snapshots considered. The PIV data contains 10 cardiac cycles with 18 instants per cycle, leading to 180 modes in total. For the CFD data, the flow field considered consists of only one cardiac cycle with 165 snapshots, resulting in 165 modes in total. The RPCA velocity field, on the other hand, consists of 180 snapshots since it was generated from PIV data, but consists of only 35 modes. This is because the RPCA process seeks to obtain a low-rank representation of the original data.

2.6. Reduced order model

To generate a low dimensional representation of the aortic flow under consideration, Eq. (9) can be applied to reconstruct the flow field from the POD modes and the mean velocity $\overline{\mathbf{u}(x, y)}$ as:

$$\mathbf{u}(x, y, t) = \overline{\mathbf{u}(x, y)} + \sum_{i=1}^{r} a_i(t)\mathbf{\Phi}_i(x, y) \tag{9}$$

where r denotes the number of modes included in the ROM. When setting $r = N$, where N denotes the total number of POD modes, Eq. (9) yields FOM. Equivalently, the reconstructed snapshot matrix $\mathbf{U}_r$ can be calculated from:

$$\mathbf{U}_r = \mathbf{\Phi}_r\mathbf{\Sigma}_r\mathbf{\Psi}_r^* \tag{10}$$

with $\mathbf{\Phi}_r$, $\mathbf{\Sigma}_r$, and $\mathbf{\Psi}_r$ are the truncated versions of $\mathbf{\Phi}$, $\mathbf{\Sigma}$, and $\mathbf{\Psi}$, respectively. The reconstruction error is defined as:

$$\varepsilon = \frac{\sum_{j=1}^{m}\sum_{i=1}^{2n} \left| \mathbf{U}(i,j) - \mathbf{U}_r(i,j) \right|}{\sum_{j=1}^{m}\sum_{i=1}^{2n} \left| \mathbf{U}(i,j) \right|} \times 100\% \tag{11}$$

The POD spatial structures and temporal coefficients were used to characterise specific flow features — *coherent structures* — in the pulsatile, aortic dissection flow, separating the periodic and random fluctuating structures from the mean flow. The spatial structures $\mathbf{\Phi}_i$ for the relevant modes were analysed by plotting the velocity fields. Then, the temporal characteristics of the flow were investigated by analysing the temporal coefficients of the most energetic POD modes in both the time and frequency domains.

Lastly, flow field reconstructions from the ROMs were performed according to Eq. (9). First $\mathbf{u}(x, y, t)$ was reconstructed using all the modes to verify the accuracy of the mathematical calculations. Then, they were reconstructed using only a selected number of modes (i.e. $\mathbf{\Phi}$1–2, $\mathbf{\Phi}$1–5, and $\mathbf{\Phi}$1–10) and the solution was compared to the original velocity fields, at different instants of the cardiac cycle, to quantify the differences.

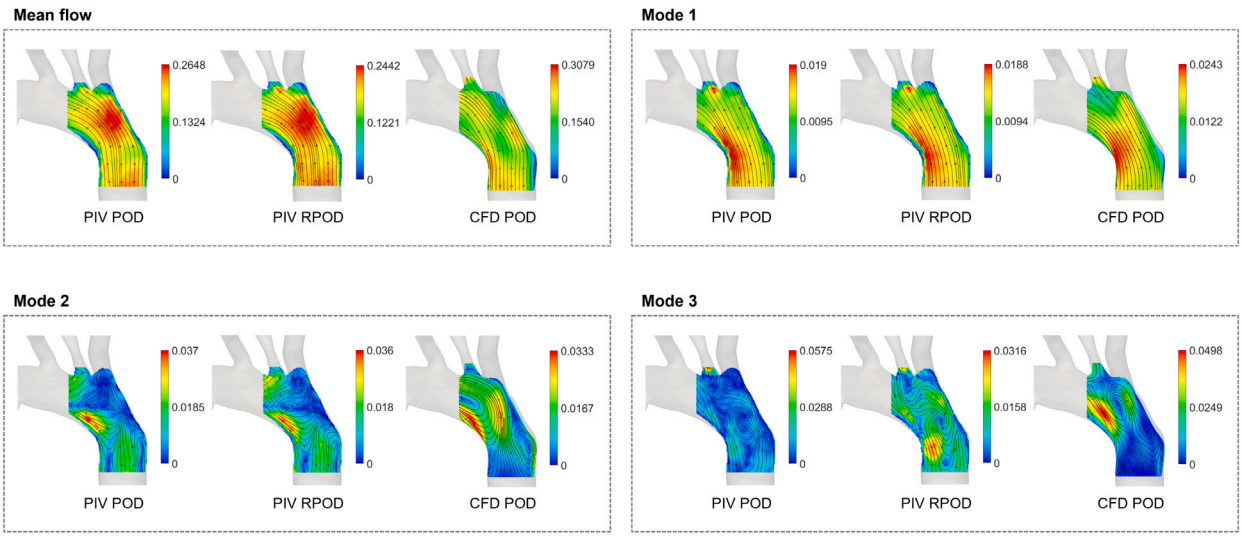

Fig. 3. The mean velocity field and the first three POD structures (Φ1–3) obtained from the PIV, RPCA, and CFD velocity fields, respectively. Super-imposed streamlines were used for illustration purposes, they do not convey any information on temporal variations. Please note that the scales of the contours are different.

Table 1
Percentage of Kinetic energy captured and reconstruction error of different groups of POD modes calculated from PIV velocity field, RPCA velocity field, and CFD velocity field.

	PIV POD		PIV RPOD		CFD POD	
Modes	Energy(%)	Error(%)	Energy(%)	Error(%)	Energy(%)	Error(%)
1–2	86.33	34.18	98.15	13.10	95.52	19.54
1–5	89.57	30.16	99.37	7.85	98.77	10.18
1–10	91.72	27.06	99.78	4.60	99.72	4.81
all	~100	~0	~100	~0	~100	~0

3. Results and discussion

3.1. Kinetic energy distribution

Table 1 lists the cumulative kinetic energy contents of the POD and RPOD modes derived from the PIV data (PIV POD, PIV RPOD respectively) compared to those derived from the CFD data (CFD POD). The energy contained in the ROMs is expressed as a percentage of the total kinetic energy in their respective FOMs, i.e. the total energy of the original or filtered PIV and CFD velocity fields respectively. While more than 90% of the kinetic energy is reached within the first 2 modes for the PIV RPOD and CFD POD data, it takes 10 modes for the PIV POD to capture that amount of energy. Similarly, Table 1 also shows that the reconstruction errors from PIV RPOD and CFD POD converge to zero faster than the ones from PIV POD.

This is not surprising as the PIV data are subject to measurement noise. In contrast, the CFD velocity field was derived from numerical computations, no measurement errors are involved. Additionally, the use of a RANS model in CFD inherently ignores turbulent fluctuations, resulting in much cleaner data compared to PIV.

The RPCA process denoises the PIV data resulting in higher cumulative energy in the first two and ten modes compared to that from PIV data alone. The energy content of each mode becomes closer to that derived from the CFD data.

3.2. POD structures and temporal coefficients

Selected POD structures (Φ1–3) are shown in Fig. 3 compared with the mean flow. All the first POD structures (Φ1) show organised motion in the same direction as the mean flow which reflects the flow at the peak systolic phase (Franzetti et al., 2022). The structures extracted from PIV POD and PIV RPOD appear to be almost identical as they represent the most energetic flow features; they slightly differ from the CFD POD ones due to the differences between the measured and computed velocity fields discussed in our previous work (Bonfanti et al., 2020).

Modes 2 and 3 (Φ2–3) exhibit more complex flow patterns characterised by re-circulation regions. As for Φ2, a high magnitude region can be seen at the inner side of the arch which reflects the flow pattern in diastole.

The temporal coefficients (a_i) of the first three POD modes are shown in Fig. 4 in the time (left column) and frequency domain (right column), respectively. The coefficients exhibit periodic characteristics in agreement with the literature (Kefayati and Poepping, 2013). The first temporal coefficient essentially reflects the shape of the patient-specific inlet flow waveform manifesting with a dominant peak in the spectra at the frequency of the cardiac cycle (f = 73.2 bpm = 1.22 Hz). As the number of modes increases, the temporal coefficients show more complicated patterns characterised by higher frequency oscillations. A second harmonic (2.44 Hz) is evident on the frequency spectra of the experimentally derived modes. This behaviour may be related to velocity fluctuations due to transitional flow. This behaviour is absent from the numerical POD coefficients which consist of one single cardiac cycle only, hence oscillating at the cardiac cycle frequency only.

3.3. Flow reconstructions

Figs. 5–7 show the comparison between the FOMs at three instants of the cardiac cycle (peak systole, deceleration and diastole), and the reconstructed velocity fields of ROMs using Φ1–2, Φ1–5 and Φ1–10. The figure also shows contours of the differences in velocity magnitude between the original and reconstructed flow fields. The reconstruction errors are shown in Table 1. As expected, in all cases, the more POD/RPOD modes are included in the reconstruction, the lower the error.

The reconstructed flow fields from the PIV POD in Fig. 5 show that good agreement can be achieved even using the first 2 POD modes at peak systole and in the descending part of the flow curve, where the flow follows relatively organised uni-directional patterns, with some differences occurring in near-wall re-circulation regions. However, more significant discrepancies are observed in diastole, both in terms of velocity magnitude, distribution and the flow directions indicated by the streamlines. Such differences are to be expected because, at diastole, the flow contains smaller vortical structures and a

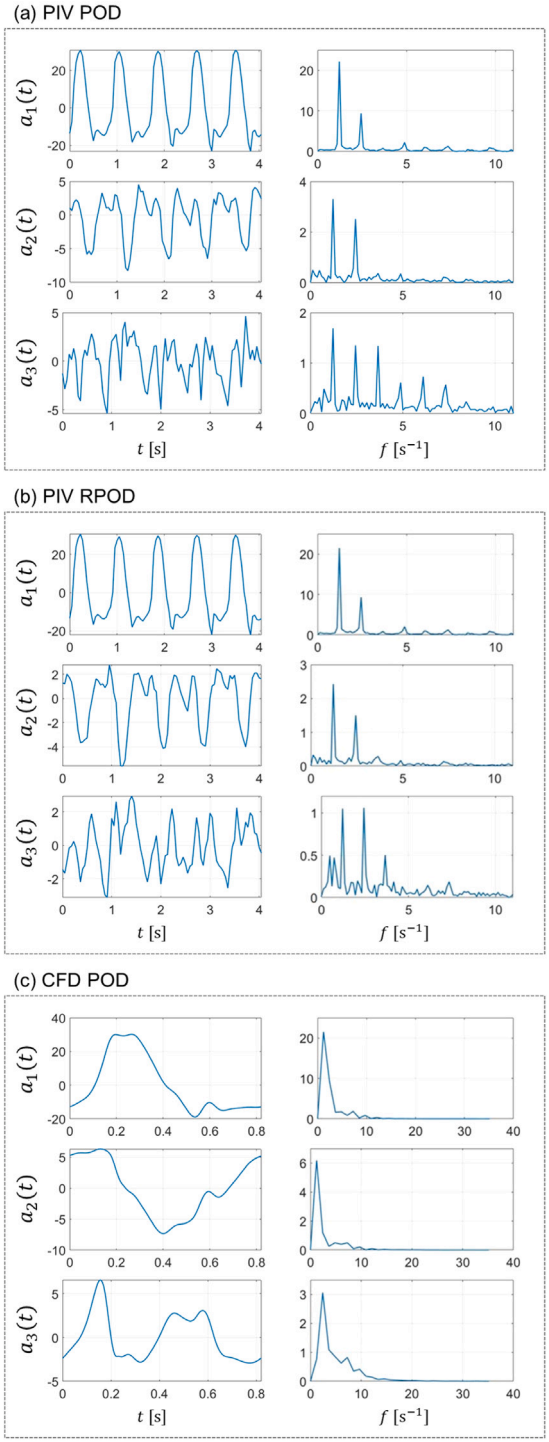

Fig. 4. The first three POD temporal coefficients (a_1, a_2, and a_3) from (a) PIV POD, (b) PIV RPOD, and (c) CFD POD presented in (left) time domain and (right) frequency domain.

more complex flow field. To fully reconstruct these structures, a higher number of modes should be included. 10 modes appear to be sufficient to reconstruct the flow at diastole accurately. When reconstructing the flow with modes Φ1–10, the maximum absolute difference is about 0.09–0.10 m/s and occurs at systole.

Similar reconstructed velocity fields are generally obtained from the PIV RPOD in Fig. 6. The only noticeable difference is at diastole, where the RPCA velocity field exhibits lower velocity magnitudes compared to the PIV-derived one, due to its filtering action. The RPCA velocity magnitude ranges from 0 to 0.2237 m/s, while the original flow field from 0 to 0.3276 m/s at diastole. When using the same number of modes to reconstruct the flow field, PIV RPOD has a much lower reconstruction error than PIV POD. The maximum absolute error when using 10 modes for the flow reconstruction is only 0.007–0.008 m/s, i.e. 10 times lower than that in PIV POD.

Finally, Fig. 7 shows that the flow reconstructions from the CFD POD analysis share similar important qualities with the experimental ones; namely that the first 2 modes are able to reconstruct the velocity field accurately at peak systole and deceleration phase, with the errors decreasing rapidly when more modes are included. The difference contour plots show less scatter compared to the PIV derived ones due to high spatial resolution of the numerical data. A maximum difference of around 0.05–0.06 m/s is found when reconstructing the flow fields using 10 modes; this is smaller than the errors in PIV POD but slightly higher than the case of PIV RPOD.

It is important to highlight that all the errors reported above are reconstruction errors. They are obtained by comparing the velocity fields from ROMs to those of their respective FOMs. These errors are not from comparisons among the PIV velocity fields, RPCA velocity fields, and CFD velocity fields (see Appendix A). Thus, they cannot be interpreted as such.

3.4. Towards personalised ROMs

The use of the RPCA algorithm in this study successfully filtered out high-frequency noise in the PIV data (see Fig. 4), improving the performance of ROMs extracted from the data. In the context of dimensionality reduction, the application of RPCA to PIV data leads to representations in a lower-dimensional space compared to the original PIV data. This feature of RPCA might be helpful when analysing the images from MR data for example, which would help pave the way towards the use of these numerical tools in a clinical setting.

However, RPOD may over-filter certain parts of the flow field as can be seen during diastole (Figs. 5–7 bottom row). While the velocity magnitude of the PIV and CFD derived fields are in the same range, it is significantly lower (by about 30%) for the RPCA derived one. This shows that the algorithm may filter out some important flow features and if implemented in a real clinical pathway, might require careful consideration. This over-filtering issue can be addressed by increasing the value of the tuning parameter λ_1. However, too high a value of λ_1 can lead to the presence of noise in the filtered data. Therefore, the main challenge involved in the application of RPCA is to find the optimal value of λ_1 that appropriately filters out the unwanted motion while preserving the relevant ones. Future work can focus on fine tuning λ_1 for a given dataset or exploring the integration of a physics-informed regularisation term into the RPCA framework to preserve the velocity signal while still reducing noise.

Nevertheless, the enhancement of *in vitro*, experimental data using RPCA demonstrated here, suggests that such methods could potentially be applied to *in vivo* data, such as 4D flow MRI, to improve their quality, making them more amenable to computational modelling and flow reconstruction (Bakhshinejad et al., 2017; Fathi et al., 2018; Töger et al., 2020) for patient-specific studies. In addition, the ability of the RPCA algorithm to effectively clean data may also result in ROMs constructed from RPOD having to include fewer modes, leading to faster computations in their subsequent applications, which is an important feature if these techniques were to be incorporated in real clinical pathways.

This work also demonstrates that it is possible to represent the behaviour of complex, pathological aortic flows using ROMs consisting of only the first few POD/RPOD modes, which shows promise in the development of more computationally efficient models to support clinical decision-making. Examples include the works of Chang et al. (2017)

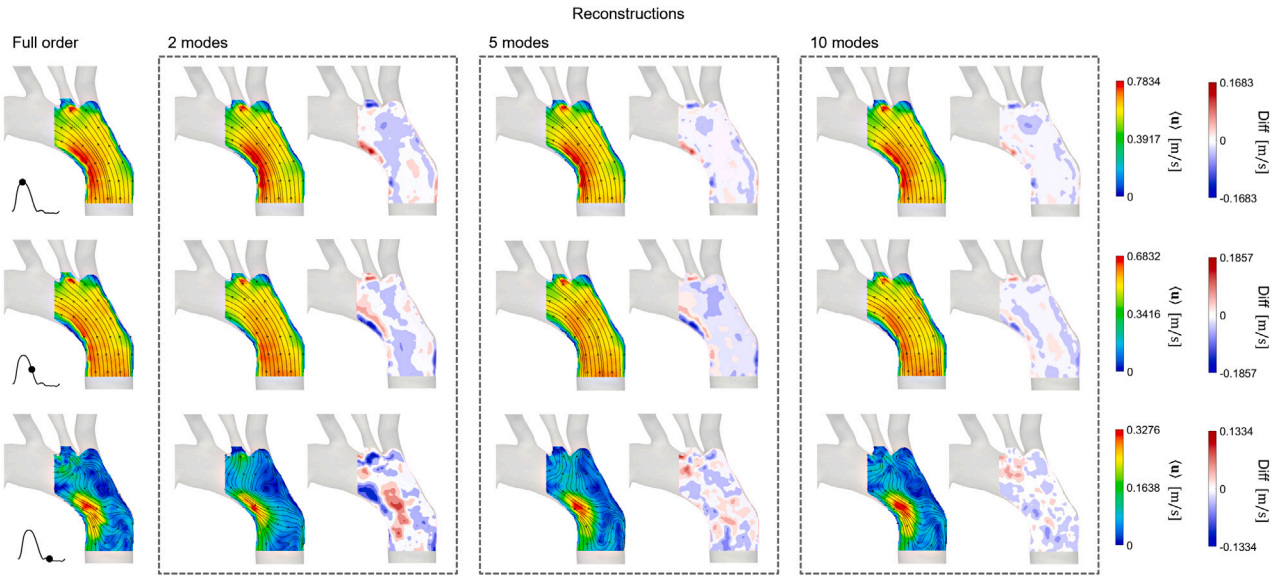

Fig. 5. PIV POD, a POD reconstruction of PIV velocity field using Φ1–2, Φ1–5, and Φ1–10. The FOM and reconstructed flow fields are visualised at three instances of the cardiac: peak systole, deceleration, and diastole. Contours showing the difference in velocity magnitude between the FOM and reconstructed flow fields are shown side by side with the reconstructed velocity field.

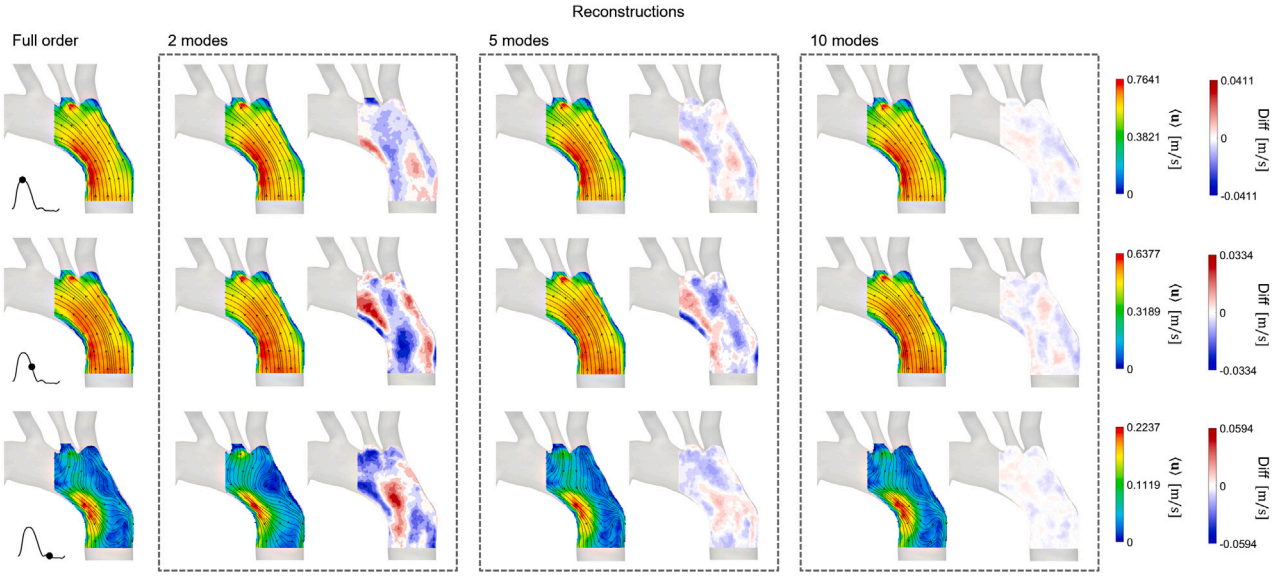

Fig. 6. PIV RPOD, a POD reconstruction of RPCA velocity field using Φ1–2, Φ1–5, and Φ1–10. The FOM and reconstructed flow fields are visualised at three instances of the cardiac: peak systole, deceleration, and diastole. Contours showing the difference in velocity magnitude between the FOM and reconstructed flow fields are shown side by side with the reconstructed velocity field.

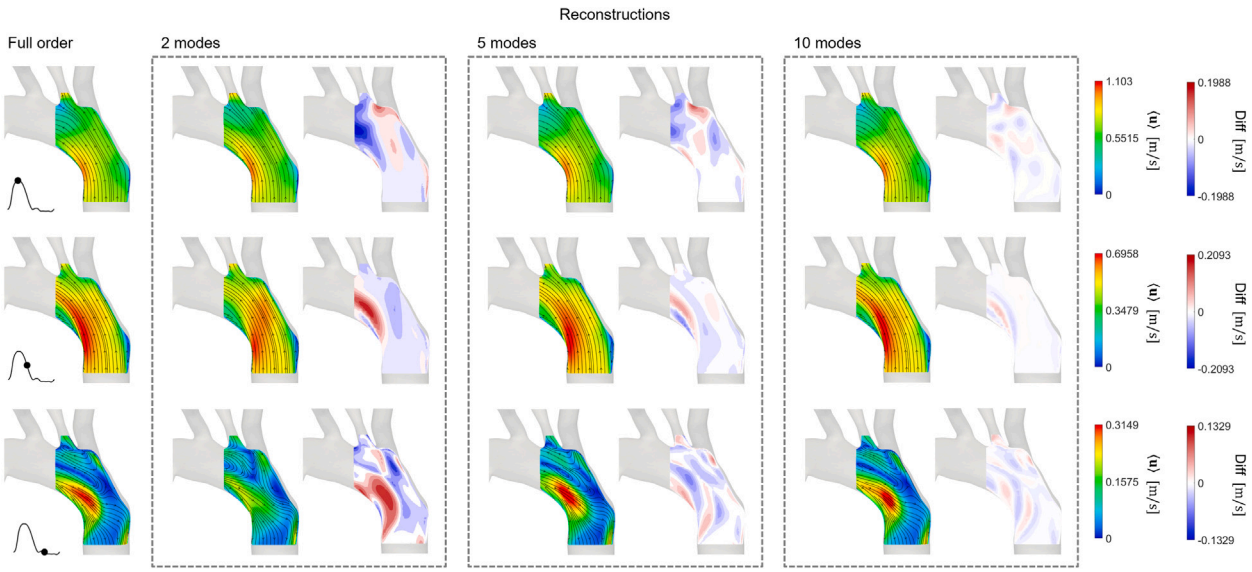

Fig. 7. CFD POD, a POD reconstruction of CFD velocity field using $\Phi 1–2$, $\Phi 1–5$, and $\Phi 1–10$. The FOM and reconstructed flow fields are visualised at three instances of the cardiac: peak systole, deceleration, and diastole. Contours showing the difference in velocity magnitude between the FOM and reconstructed flow fields are shown side by side with the reconstructed velocity field.

who developed a computationally efficient ROM to study the flow patterns and the WSS distribution in simplified models of an abdominal aortic aneurysm, and Buoso et al. (2019), who developed ROMs of blood flow for non-invasive functional evaluation of the pressure drop in coronary artery disease using parameterised POD. ROMs may also possess properties that can serve as supplementary haemodynamic indices. For example, by monitoring the temporal evolution of energy distribution, it may be possible to track the progression of some cardiovascular diseases or even vascular remodelling. Moreover, the energy fraction associated with higher-order POD/RPOD modes may contain information that can be used to fine-tune turbulence parameters when modelling vascular flows.

Finally, ROMs can also be combined with rapidly evolving machine learning tools to allow for *optimisation* and *design* in fluid mechanics, moving towards real-time modelling. This would allow, for instance, the study of a wide range of parameters for a given vascular pathology (e.g. increasing or decreasing the level of stenosis on coronary disease or coarctations) and to analyse the consequences on the flow and pressure fields, which could serve as an initial step to investigate patient-specific pre-interventional options (Siena et al., 2023; Pajaziti et al., 2023; Liang et al., 2020).

4. Conclusions

The time-dependent flow in an aortic model, measured by PIV, was enhanced by RPCA and decomposed by means of POD to create ROMs. The decomposed flows were compared against those from numerical data obtained for the same patient-specific conditions. The first two modes derived from RPOD capture more than 90% of the kinetic energy, in agreement with the corresponding CFD derived ROMs.

The large and small-scale structures within the flow, corresponding to more or less energetic modes, were evaluated and described by means of POD/RPOD spatial structures and POD/RPOD temporal coefficients. By combining only the most energetic modes to represent the flow, it was shown that complex, time-dependent haemodynamic data can be represented with simpler low-dimensional models based on a small number of spatial modes. This combined with the strong reconstruction performance of RPOD, illustrates the potential of the approach to enhance the quality of measurements and to develop more computationally efficient models for clinical application.

CRediT authorship contribution statement

Chotirawee Chatpattanasiri: Writing – original draft, Visualization, Methodology, Investigation, Formal analysis, Conceptualization. **Gaia Franzetti:** Writing – original draft, Visualization, Methodology, Investigation, Formal analysis, Conceptualization. **Mirko Bonfanti:** Software, Investigation. **Vanessa Diaz-Zuccarini:** Writing – review & editing, Supervision Resources, Project administration, Funding acquisition, Conceptualization. **Stavroula Balabani:** Writing – review & editing, Supervision, Resources, Project administration, Funding acquisition, Conceptualization.

Declaration of competing interest

The authors declare that they have no known competing financial interests or personal relationships that could have appeared to influence the work reported in this paper.

Acknowledgments

This project was supported by the Wellcome/EPSRC Centre for Interventional and Surgical Sciences (WEISS) (203145Z/16/Z); EPSRC Transformative Healthcare Technologies (EP/W00481X/1); British Heart Foundation (FS/15/22/31356, NH/20/1/34705); UCLH Biomedical Research Centre (GA BRC636b/HEI/SB/1104); and the Department of Mechanical Engineering, University College London. The authors would also like to thank Dr. Tom Lacassagne and Dr. Andrea Ducci for their constructive feedback.

Appendix A. Comparison of velocity fields between CFD and PIV before and after RPCA

The comparisons of PIV, RPCA, and CFD velocity fields is shown in Fig. A.1. Fig. A.1a shows the velocity magnitude of the mean flow in the three velocity fields with four straight lines. A closer comparison

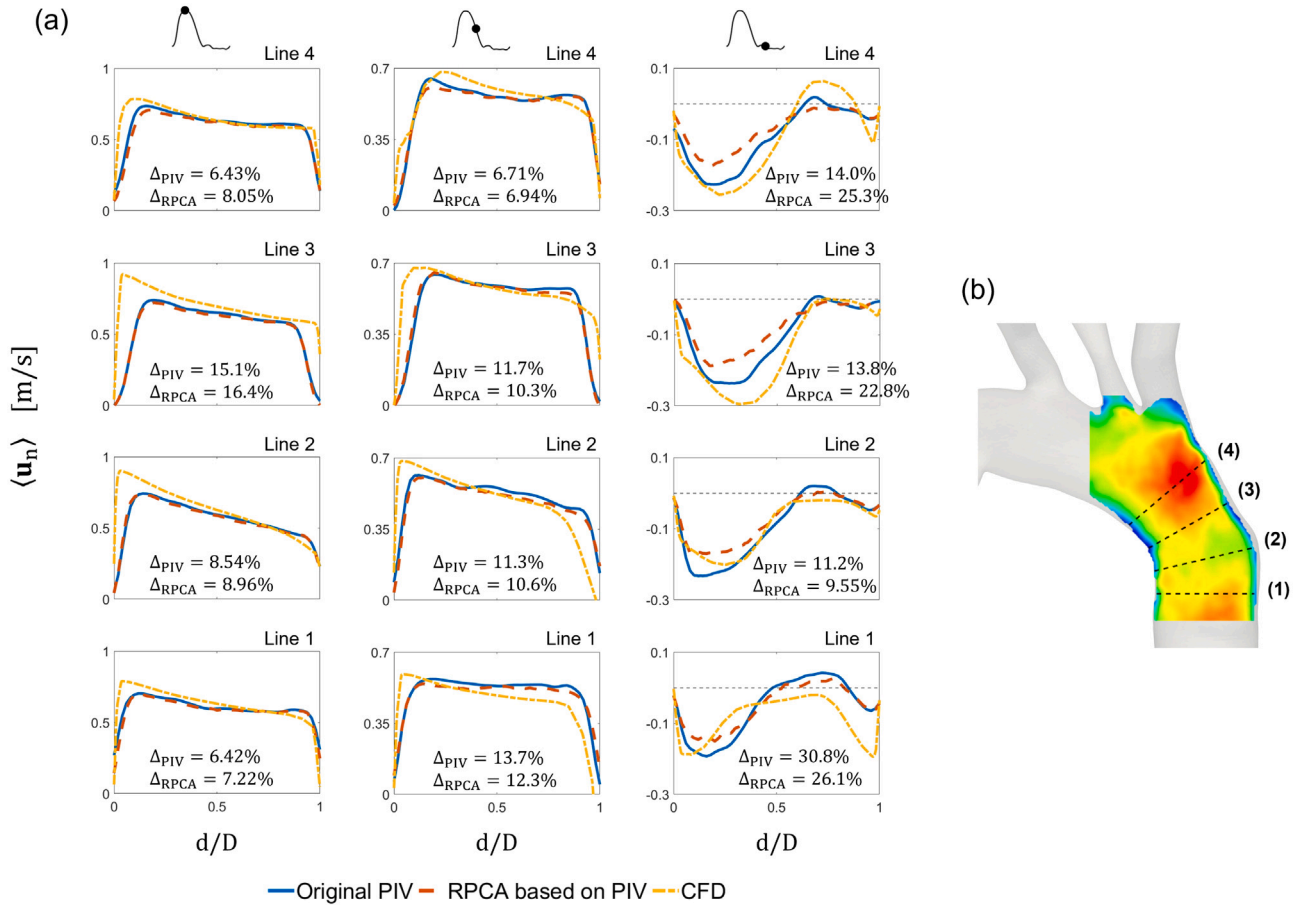

Fig. A.1. (a) Comparison of axial velocity profiles obtained from experimental PIV data before RPCA, after RPCA, and CFD data. (b) Four lines across the aortic arch where the velocity profiles were measured.

between the three velocity fields is provided in Fig. A.1b by plotting the axial velocity profiles ($\langle \mathbf{u}_n \rangle$) over those four selected lines.

The percentage difference is calculated in the same way as in Bonfanti et al. (2020):

$$\Delta = \frac{1}{N}\sum_{i=1}^{N}\frac{\left|u^e_{n,j} - u^c_{n,j}\right|}{\max_j\left|u^c_{n,j}\right|} \tag{12}$$

where $u^c_{n,i}$ is the CFD velocity profile. When calculating Δ_{PIV}, $u^e_{n,i}$ is the PIV velocity profile, and when calculating Δ_{RPCA}, $u^e_{n,i}$ is the RPCA velocity profile. It should be noted that the percentage differences are not exactly the same as those reported in Bonfanti et al. (2020) because there might be discrepancies in the locations of the four lines.

As shown from the above (Fig. A.1b), RPCA may not always bring the PIV and CFD closer together in terms of the actual velocity values due to the over-filtering behaviour discussed in Section 3.4. However, RPCA leads to PIV derived ROMs that capture the same percentage of energy as CFD ones when reconstructing with the same number of modes (Table 1). To help visualise the effect of RPCA on PIV data, comparison can be found in the video file attached (or here).

Appendix B. Normalised POD/RPOD coefficients

The relation between the first coefficients a_i was investigated by plotting the space (a^*_1, a^*_2), calculated as:[4]

$$\tilde{a}_i = \frac{a_i}{\sqrt{2\lambda_i}} \tag{13}$$

and normalise as

$$a^*_i = \frac{2(\tilde{a}_i - \min(\tilde{a}_i))}{(\max(\tilde{a}_i) - \min(\tilde{a}_i))} - 1 \tag{14}$$

The normalised temporal coefficients a^*_1, a^*_2 and a^*_3, are plotted against each other in Fig. B.1. The phase-averaged coefficients for the experimental data are also indicated in blue. They exhibit organised, closed-loop structures, indicating periodicity similar to the CFD data.

The 2D plots of a^*_1 and a^*_2 in Fig. B.1 do not show a clear circular or elliptic pattern, implying that the first two POD modes do not form a pair. The plots also indicate the same behaviour for the first two PIV POD and PIV RPOD coefficients which slightly differs from the CFD POD ones.

An interesting observation arises when investigating the relation amongst the first three coefficients (a^*_1, a^*_2 and a^*_3). The plots on the right side of Fig. B.1a–c show a more complex organisation amongst these modes. This behaviour highlights the interdependent relationships and energy transfer between the first three modes and may correspond to energy transfer amongst different periodic structures (with different energy contents and frequency profiles) within the flow field. A similar *'triadic interaction'* has been reported by Gabelle et al. (2017) in a stirred tank flow (who attributed the behaviour to non-linear interactions between the modes), and by Lacassagne et al. (2021) in an oscillating grid flow.

[4] This approach has been used in different studies, for example see Imomoh et al. (2010) and Ducci et al. (2008).

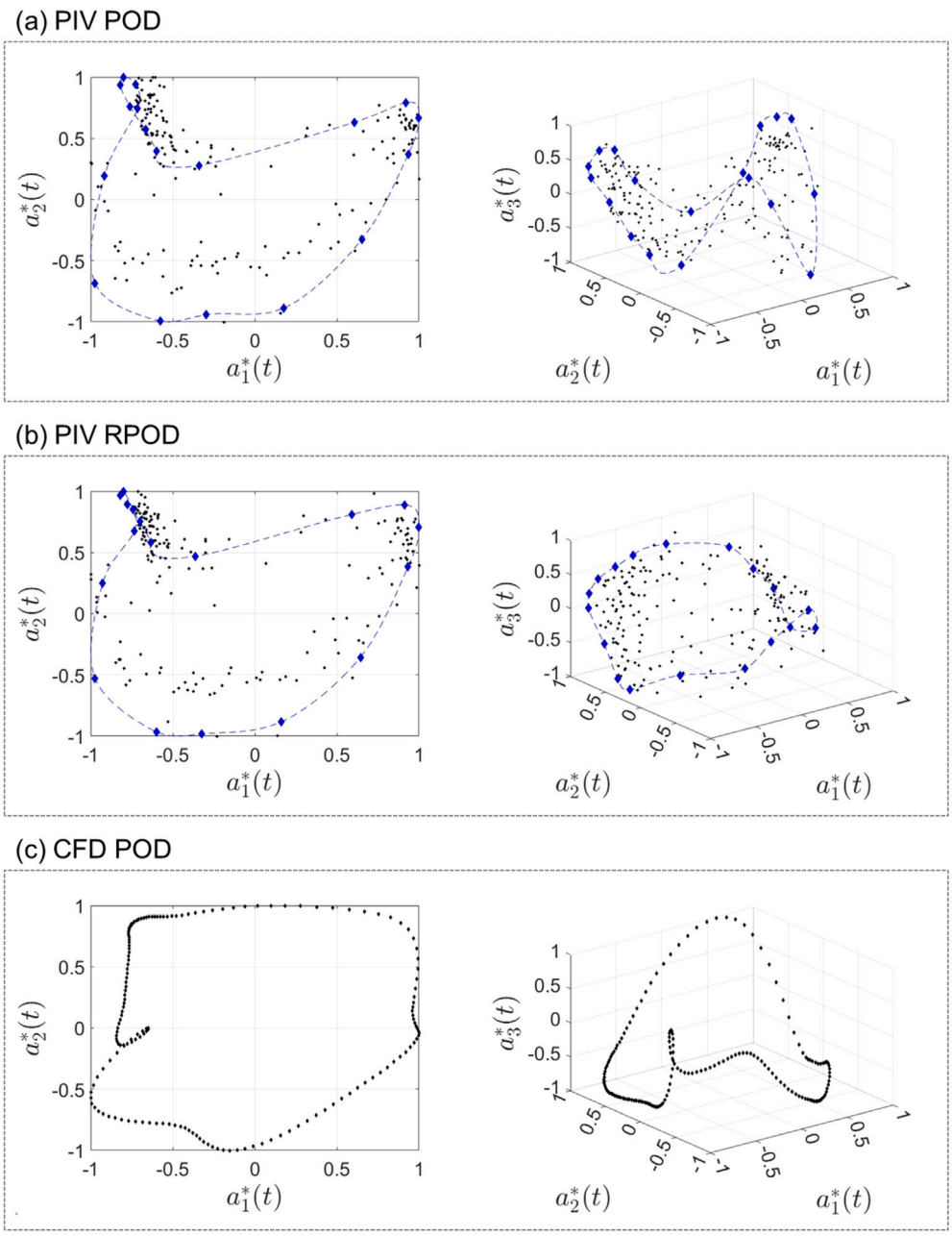

Fig. B.1. Scatter plots of normalised POD coefficients (left) a_1^* and a_2^* and (right) a_1^*, a_2^* and a_3^* computed from (a) PIV POD, (b) PIV RPOD, and (c) CFD POD. The black points represent the coefficients for all the modes, whilst the blue ones represent the phase-averaged POD modes. The blue lines connect the phase-averaged coefficients for better visualisation. (For interpretation of the references to color in this figure legend, the reader is referred to the web version of this article.)

Appendix C. Supplementary data

Supplementary material related to this article can be found online at https://doi.org/10.1016/j.jbiomech.2023.111759.

References

Arzani, A., Dawson, S.T.M., 2021. Data-driven cardiovascular flow modelling: Examples and opportunities. J. R. Soc. Interface 18 (175), 20200802. http://dx.doi.org/10.1098/rsif.2020.0802.

Baghaie, A., 2019. Robust principal component analysis for background estimation of particle image velocimetry data. In: 2019 IEEE Long Island Systems, Applications and Technology Conference. LISAT, pp. 1–6. http://dx.doi.org/10.1109/LISAT.2019.8817345.

Bakhshinejad, A., Baghaie, A., Vali, A., Saloner, D., Rayz, V.L., D'Souza, R.M., 2017. Merging computational fluid dynamics and 4D flow MRI using proper orthogonal decomposition and ridge regression. J. Biomech. 58, 162–173. http://dx.doi.org/10.1016/j.jbiomech.2017.05.004.

Ballarin, F., Faggiano, E., Ippolito, S., Manzoni, A., Quarteroni, A., Rozza, G., Scrofani, R., 2016. Fast simulations of patient-specific haemodynamics of coronary artery bypass grafts based on a POD-Galerkin method and a vascular shape parametrization. J. Comput. Phys. 315, 609–628. http://dx.doi.org/10.1016/j.jcp.2016.03.065.

Berkooz, G., Holmes, P., Lumley, J.L., 1993. The proper orthogonal decomposition in the analysis of turbulent flows. Annu. Rev. Fluid Mech. 25 (1), 539–575. http://dx.doi.org/10.1146/annurev.fl.25.010193.002543.

Bonfanti, M., Balabani, S., Alimohammadi, M., Agu, O., Homer-vanniasinkam, S., Díaz-zuccarini, V., 2018. A simplified method to account for wall motion in patient-specific blood flow simulations of aortic dissection : Comparison with fluid-structure interaction. Med. Eng. Phys. 58, 72–79. http://dx.doi.org/10.1016/j.medengphy.2018.04.014.

Bonfanti, M., Franzetti, G., Homer-Vanniasinkam, S., Diaz-Zuccarini, V., Balabani, S., 2020. A combined in vivo, in vitro, in silico approach to study the patient-specific

haemodynamics of Type-B aortic dissections. Ann. Biomed. Eng. 48, 2950—-2964. http://dx.doi.org/10.1007/s10439-020-02603-z.

Brunton, S.L., Kutz, J.N., 2019. Data-Driven Science and Engineering: Machine Learning, Dynamical Systems, and Control. Cambridge University Press, http://dx.doi.org/10.1017/9781108380690.

Buoso, S., Manzoni, A., Alkadhi, H., Plass, A., Quarteroni, A., Kurtcuoglu, V., 2019. Reduced-order modeling of blood flow for noninvasive functional evaluation of coronary artery disease. Biomech. Model. Mechanobiol. 18 (6), 1867–1881. http://dx.doi.org/10.1007/s10237-019-01182-w.

Byrne, G., Mut, F., Cebral, J., 2014. Quantifying the large-scale hemodynamics of intracranial aneurysms. Am. J. Neuroradiol. 35 (2), 333–338. http://dx.doi.org/10.3174/ajnr.A3678.

Candès, E.J., Li, X., Ma, Y., Wright, J., 2011. Robust principal component analysis? J. ACM 58 (3), 1–37. http://dx.doi.org/10.1145/1970392.1970395.

Chang, G.H., Schirmer, C.M., Modarres-Sadeghi, Y., 2017. A reduced-order model for wall shear stress in abdominal aortic aneurysms by proper orthogonal decomposition. J. Biomech. 54, 33–43. http://dx.doi.org/10.1016/j.jbiomech.2017.01.035.

Chinesta, F., Ammar, A., Leygue, A., Keunings, R., 2011. An overview of the proper generalized decomposition with applications in computational rheology. J. Non-Newton. Fluid Mech. 166 (11), 578–592. http://dx.doi.org/10.1016/j.jnnfm.2010.12.012.

Di Labbio, G., Kadem, L., 2019. Reduced-order modeling of left ventricular flow subject to aortic valve regurgitation. Phys. Fluids 31 (3), 031901. http://dx.doi.org/10.1063/1.5083054.

Ducci, A., Doulgerakis, Z., Yianneskis, M., 2008. Decomposition of flow structures in stirred reactors and implications for mixing enhancement. Ind. Eng. Chem. Res. 47 (10), 3664–3676. http://dx.doi.org/10.1021/ie070905m.

Eivazi, H., Le Clainche, S., Hoyas, S., Vinuesa, R., 2022. Towards extraction of orthogonal and parsimonious non-linear modes from turbulent flows. Expert Syst. Appl. 202, 117038. http://dx.doi.org/10.1016/j.eswa.2022.117038.

Farahbakhsh, I., 2020. Krylov Subspace Methods with Application in Incompressible Fluid Flow Solvers. John Wiley & Sons, http://dx.doi.org/10.1002/9781119618737.

Fathi, M.F., Bakhshinejad, A., Baghaie, A., Saloner, D., Sacho, R.H., Rayz, V.L., D'Souza, R.M., 2018. Denoising and spatial resolution enhancement of 4D flow MRI using proper orthogonal decomposition and lasso regularization. Comput. Med. Imaging Graph. 70, 165–172. http://dx.doi.org/10.1016/j.compmedimag.2018.07.003.

Febina, J., Sikkandar, M.Y., Sudharsan, N.M., 2018. Wall shear stress estimation of thoracic aortic aneurysm using computational fluid dynamics. Comput. Math. Methods Med. 2018, 7126532. http://dx.doi.org/10.1155/2018/7126532.

Franzetti, G., Bonfanti, M., Homer-Vanniasinkam, S., Diaz-Zuccarini, V., Balabani, S., 2022. Experimental evaluation of the patient-specific haemodynamics of an aortic dissection model using particle image velocimetry. J. Biomech. 134, 110963. http://dx.doi.org/10.1016/j.jbiomech.2022.110963.

Franzetti, G., Díaz-Zuccarini, V., Balabani, S., 2019. Design of an in vitro mock circulatory loop to reproduce patient-specific vascular conditions: Toward precision medicine. J. Eng. Sci. Med. Diagn. Ther. 2 (4), 041004. http://dx.doi.org/10.1115/1.4044488.

Gabelle, J.C., Morchain, J., Liné, A., 2017. Kinetic energy transfer between first proper orthogonal decomposition modes in a mixing tank. Chem. Eng. Technol. 40 (5), 927–937. http://dx.doi.org/10.1002/ceat.201600674.

Han, S., Schirmer, C.M., Modarres-Sadeghi, Y., 2020. A reduced-order model of a patient-specific cerebral aneurysm for rapid evaluation and treatment planning. J. Biomech. 103, 109653. http://dx.doi.org/10.1016/j.jbiomech.2020.109653.

Hellmeier, F., Nordmeyer, S., Yevtushenko, P., Bruening, J., Berger, F., Kuehne, T., Goubergrits, L., Kelm, M., 2018. Hemodynamic evaluation of a biological and mechanical aortic valve prosthesis using patient-specific MRI-based CFD. Artif. Organs 42 (1), 49–57. http://dx.doi.org/10.1111/aor.12955.

Imomoh, E., Dusting, J., Balabani, S., 2010. On the quasiperiodic state in a moderate aspect ratio Taylor-Couette flow. Phys. Fluids 22 (4), 1–10. http://dx.doi.org/10.1063/1.3407665.

Javadzadegan, A., Moshfegh, A., Afrouzi, H.H., Omidi, M., 2018. Magnetohydrodynamic blood flow in patients with coronary artery disease. Comput. Methods Programs Biomed. 163, 111–122. http://dx.doi.org/10.1016/j.cmpb.2018.06.007.

Kefayati, S., Poepping, T.L., 2013. Transitional flow analysis in the carotid artery bifurcation by proper orthogonal decomposition and particle image velocimetry. Med. Eng. Phys. 35 (7), 898–909. http://dx.doi.org/10.1016/j.medengphy.2012.08.020.

Lacassagne, T., Simoëns, S., El Hajem, M., Champagne, J.-Y., 2021. POD analysis of oscillating grid turbulence in water and shear thinning polymer solution. AIChE J. 67 (1), e17044. http://dx.doi.org/10.1002/aic.17044.

Liang, Y., Lee, H., Lim, S., Lin, W., Lee, K., Wu, C., 2002. Proper orthogonal decomposition and its applications—Part I: Theory. J. Sound Vib. 252 (3), 527–544. http://dx.doi.org/10.1006/jsvi.2001.4041.

Liang, L., Mao, W., Sun, W., 2020. A feasibility study of deep learning for predicting hemodynamics of human thoracic aorta. J. Biomech. 99, 109544. http://dx.doi.org/10.1016/j.jbiomech.2019.109544.

Murata, T., Fukami, K., Fukagata, K., 2020. Nonlinear mode decomposition with convolutional neural networks for fluid dynamics. J. Fluid Mech. 882, A13. http://dx.doi.org/10.1017/jfm.2019.822.

Pajaziti, E., Montalt-Tordera, J., Capelli, C., Sivera, R., Sauvage, E., Schievano, S., Quail, M., Muthurangu, V., 2023. Shape-driven deep neural networks for fast acquisition of aortic 3D pressure and velocity flow fields. PLOS Comput. Biol. 19 (4), 1–20. http://dx.doi.org/10.1371/journal.pcbi.1011055.

Quarteroni, A., Rozza, G., 2007. Numerical solution of parametrized Navier–Stokes equations by reduced basis methods. Numer. Method. Partial Differ. Equasion 23 (4), 904–922. http://dx.doi.org/10.1002/num.20249.

Rigatelli, G., Chiastra, C., Pennati, G., Dubini, G., Migliavacca, F., Zuin, M., 2021. Applications of computational fluid dynamics to congenital heart diseases: A practical review for cardiovascular professionals. Expert Rev. Cardiovasc. Ther. 19 (10), 907–916. http://dx.doi.org/10.1080/14779072.2021.1999229.

Scherl, I., Strom, B., Shang, J.K., Williams, O., Polagye, B.L., Brunton, S.L., 2020. Robust principal component analysis for modal decomposition of corrupt fluid flows. Phys. Rev. Fluids 5 (5), 054401. http://dx.doi.org/10.1103/PhysRevFluids.5.054401.

Schmid, P.J., 2021. Annual review of fluid mechanics dynamic mode decomposition and its variants. Annu. Rev. Fluid Mech. 54, 225–254. http://dx.doi.org/10.1146/annurev-fluid-030121-015835.

Siena, P., Girfoglio, M., Ballarin, F., Rozza, G., 2023. Data-driven reduced order modelling for patient-specific hemodynamics of coronary artery bypass grafts with physical and geometrical parameters. J. Sci. Comput. 94 (2), 1–30. http://dx.doi.org/10.1007/s10915-022-02082-5.

Stokes, C., Bonfanti, M., Li, Z., Xiong, J., Chen, D., Balabani, S., Díaz-Zuccarini, V., 2021. A novel MRI-based data fusion methodology for efficient, personalised, compliant simulations of aortic haemodynamics. J. Biomech. 129, 110793. http://dx.doi.org/10.1016/j.jbiomech.2021.110793.

Stokes, C., Haupt, F., Becker, D., Muthurangu, V., von Tengg-Kobligk, H., Balabani, S., Díaz-Zuccarini, V., 2023. The influence of minor aortic branches in patient-specific flow simulations of Type-B aortic dissection. Ann. Biomed. Eng. 51 (7), 1627–1644. http://dx.doi.org/10.1007/s10439-023-03175-4.

Töger, J., Zahr, M.J., Aristokleous, N., Markenroth Bloch, K., Carlsson, M., Persson, P.O., 2020. Blood flow imaging by optimal matching of computational fluid dynamics to 4D-flow data. Magn. Reson. Med. 84 (4), 2231–2245. http://dx.doi.org/10.1002/mrm.28269.

Wang, Y., Yao, H., Zhao, S., 2016. Auto-encoder based dimensionality reduction. Neurocomputing 184, 232–242. http://dx.doi.org/10.1016/j.neucom.2015.08.104.